Aerosol Science and Technology 33:49–70 (2000)

Published by Taylor and Francis
0278-6826 / 00 / $12.00 + .00

Development of an Aerosol Mass Spectrometer for Size and Composition Analysis of Submicron Particles

John T. Jayne, Danna C. Leard, Xuefeng Zhang, Paul Davidovits, Kenneth A. Smith, Charles E. Kolb, and Douglas R. Worsnop

CENTER FOR AEROSOL AND CLOUD CHEMISTRY, AERODYNE RESEARCH, INC, 45 MANNING ROAD BILLERICA, MA (J.T.J., D.R.W., C.E.K.), DEPARTMENT OF CHEMISTRY, BOSTON COLLEGE, CHESTNUT HILL, MA (D.C.L, P.D.), DEPARTMENT OF CHEMICAL ENGINEERING, MASSACHUSETTS INSTITUTE OF TECHNOLOGY, CAMBRIDGE, MA (X.Z., K.A.S.)

ABSTRACT. The importance of atmospheric aerosols in regulating the Earth's climate and their potential detrimental impact on air quality and human health has stimulated the need for instrumentation which can provide real-time analysis of size resolved aerosol, mass, and chemical composition. We describe here an aerosol mass spectrometer (AMS) which has been developed in response to these aerosol sampling needs and present results which demonstrate quantitative measurement capability for a laboratory-generated pure component NH_4NO_3 aerosol. The instrument combines standard vacuum and mass spectrometric technologies with recently developed aerosol sampling techniques. A unique aerodynamic aerosol inlet (developed at the University of Minnesota) focuses particles into a narrow beam and efficiently transports them into vacuum where aerodynamic particle size is determined via a particle time-of-flight (TOF) measurement. Time-resolved particle mass detection is performed mass spectrometrically following particle flash vaporization on a resistively heated surface. Calibration data are presented for aerodynamic particle velocity and particle collection efficiency measurements. The capability to measure aerosol size and mass distributions is compared to simultaneous measurements using a differential mobility analyzer (DMA) and condensation particle counter (CPC). Quantitative size classification is demonstrated for pure component NH_4NO_3 aerosols having mass concentrations $> \sim 0.25$ µg m^{-3}. Results of fluid dynamics calculations illustrating the performance of the aerodynamic lens are also presented and compared to the measured performance. The utility of this AMS as both a laboratory and field portable instrument is discussed.

INTRODUCTION

Aerosols play important roles in atmospheric chemistry, industrial processes, and biological respiration. An improved understanding of anthropogenic particulate emissions has caused increased awareness and concern about the impact of aerosols on climate, air quality, and human heath. Particle loadings, aerosol size distributions, and compositions all need to be known. Many questions concerning the nature of aerosol formation, transport, and effect remain largely unanswered, particularly with regard to the human health issue. The new US EPA PM 2.5 standard is quite controversial since it is based solely on the mass loading (Henry 1998). More extensive studies from both laboratory and field experiments are required in order to devise rational control strategies.

Much of the current uncertainty concerning aerosol impact on climate and human health is due to the lack of instrumentation which is capable of providing both particle size distributions and chemical composition in real time. Typically, such information has been obtained from cascade impactors which require many hours of sampling followed by costly post-collection chemical analysis techniques. While such an approach allows many of the already established analytical laboratory techniques for chemical analysis to be applied, questions regarding original particle composition arise due to possible chemical transformations on the impactor surface and losses due to component volatility.

Recently, several groups have developed instrumentation capable of performing real-time on-line size and composition analysis of single particles. Most of these techniques involve the use of a high power laser to vaporize and ionize the aerosol particle, followed by mass spectrometric analysis (Gard et al. 1997; Reilly et al. 1998; Hinz et al. 1996; Carson et al. 1995; Murphy et al. 1995). These laser-based single particle instruments all require laser triggering circuitry, which is usually in the form of an optical signal generated by single particle scattering of a visible laser beam. This approach requires that the particle to be detected be sufficiently large ($> \sim 0.2$ μm) to efficiently scatter the visible light. Particle size information is obtained in some cases by measuring particle time-of-flight (TOF) in vacuum using two light scattering signals (Salt et al. 1996) or in other cases by measuring the intensity of the scattered light (Murphy and Thomson 1995) or by using separate aerosol sizing instrumentation.

These laser-based instruments are impressive and field versions have already made significant contributions towards better characterizing aerosol sources and aerosol chemical processing (see, for example, Noble and Prather 1996; Noble and Prather 1997; Silva and Prather 1997; Liu et al. 1997; Reilly et al. 1998; Murphy and Thomson 1997a, b; Murphy et al. 1999).

An important aspect of a real-time aerosol instrument is the sampling inlet. Quantitatively delivering ambient aerosol into the vacuum system is just as important as quantitatively detecting and sizing a particle so that particle size distributions can be accurately reported. A unique aerodynamic aerosol sampling lens has been described by Liu et al. (1995a, b), which operates with high particle transmission efficiencies. An appropriately designed lens system focuses particles into a narrow beam as they enter into vacuum with nearly 100% transmission efficiency. Such a lens system has been used in a particle beam mass spectrometer by Ziemann et al. (1995) for measuring particle size distributions, and more recently one has been designed for generating particle beams from stratospheric pressures for stratospheric aerosol sampling (Schreiner et al. 1998).

Our approach to developing an aerosol mass spectrometer builds on earlier efforts at performing particle mass spectrometric detection using resistively heated surfaces as the particle vaporization source (Allen and Gould 1981 and Sinha et al. 1982). The aerosol mass spectrometer (AMS) described here combines the high performance aerosol sampling inlet of the Liu et al. (1995a, b) design with particle detection via efficient thermal vaporization. In this approach, particles are focused into a narrow beam while being sampled into vacuum and directed onto a resistively heated surface. The volatile and semivolatile components in/on the particle flash vaporize upon contact in the heater; the molecular constituents are then ionized by electron impaction and analyzed as positive ions using standard quadrupole mass spectrometry. Fast particle detection synchronized with a mechanical particle beam chopper allows particle size to be determined by a particle TOF measurement when sufficient mass is present for detection. This paper describes the operation and calibration of this prototype instrument.

INSTRUMENT DESCRIPTION

An instrument schematic is shown in Figure 1. It consists of three main sections: (1) an aerosol sampling chamber, (2) a particle sizing chamber, and (3) a particle composition detection chamber. Each chamber is separated by critical apertures and is differentially pumped. A portable instrument currently under construction measures approximately 5″ × 5″ × 24″, not including the vacuum pumps. A description of each of the major components is presented below.

Aerosol Sampling Chamber

The aerosol sampling chamber couples the aerodynamic particle beam-forming lens (Liu et al. 1995a, b) to the vacuum system. The lens tube consists of six precision machined orifice lenses ranging from 5 mm id

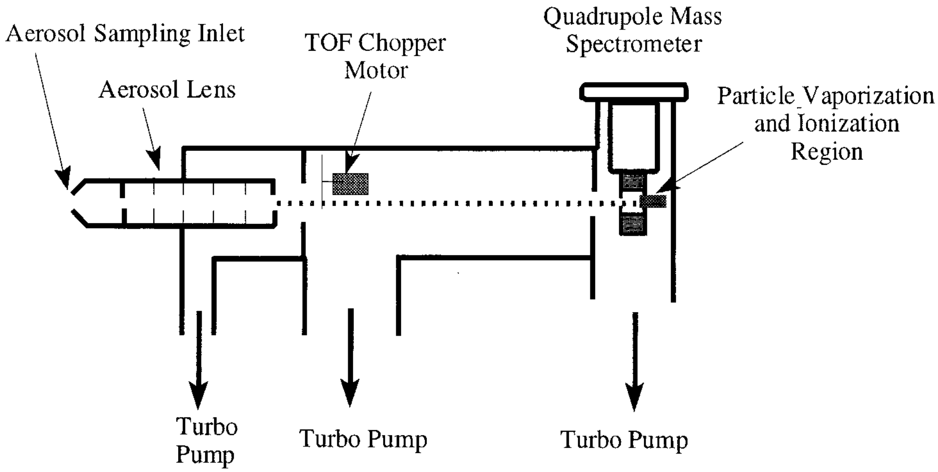

FIGURE 1. AMS for size and composition analysis of submicron aerosol. Ambient pressure aerosol is sampled into vacuum using an aerodynamic lens. Aerodynamic particle size is determined from a particle TOF measurement. Size resolved composition is measured by a quadrupole mass spectrometer following particle flash vaporization on a resistively heated surface and electron impact ionization of the vaporized species.

at the entrance to 3 mm id at the exit, which are all mounted in a precision bore stainless steel tube (nominally 1/2″ OD × 12″ in length). In one version of the instrument the lens tube is mounted to the vacuum chamber on an X-Y translation/tilt stage providing a means of diagnosing beam quality by manipulating beam alignment. The lens focuses particles into a narrow beam (~ 1 mm diameter) with nearly 100% particle transmission efficiency to the detector for particles in the size range between 70 and 500 nm in diameter. Ambient pressure particle-laden air is pumped through this lens into the vacuum system. The aerosol inlet used here operates efficiently with ~ 2 torr pressure at the inlet. A 100 μm diameter pressure drop orifice mounted at the inlet of the aerosol lens is used to fix the inlet pressure and the gas flow rate (~ 100 sccm). The 100 μm diameter pressure drop orifice is mounted upstream of the entrance of the lens tube separated by a 10 cm section of 1/2″ OD tubing. A 250 L/s turbomolecular pump is used to evacuate the aerosol sampling chamber and maintain the flow through the aerosol lens. The pressure in this chamber is maintained below 10^{-3} torr.

The performance of the aerodynamic lens has been modeled using a commercially available fluid dynamics program (FLUENT 1995). Calculations describing the particle focusing capability, the particle transmission efficiency, and the size-dependent particle velocities generated by the aerodynamic inlet have been performed and support the results of the measured lens performance. One example calculation is shown in Figure 2 which plots particle trajectories through the lens for 100 nm diameter spheres which have a density of 1 gm cm^{-3}. Each line in the figure is the trajectory for particles initialized at a particular radial coordinate. The figure illustrates the focusing action of the lens system and also shows the actual dimensions of the lens tube used in the AMS. The calculations are for initial conditions of 97.3 sccm of dry air at 295 K, corresponding to the measured gas flow rate through the 100 μm diameter aperture, and 2.1 torr at the inlet, which is the measured pressure.

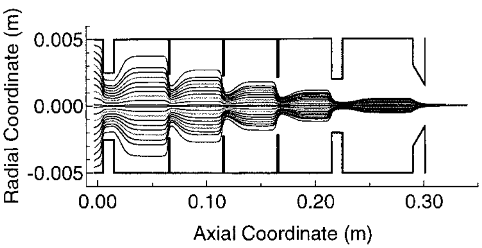

FIGURE 2. FLUENT simulation results illustrating the focusing action of the aerodynamic particle beam forming lens. Curved lines are the particle trajectories for particles entering at different radial coordinates. The results displayed are for 100 nm diameter spheres with a density of 1 gm cm^{-3} at typical lens inlet pressure (2.1 torr) and volumetric flow rate (97.3 sccm). The figure also shows the physical dimensions of the lens system.

The first five plate apertures serve to focus the particles onto the center line; the final exit aperture controls supersonic gas expansion and particle acceleration into the vacuum system. During the gas expansion, particles acquire a distribution of velocities; smaller diameter particles accelerate to faster velocities and larger diameter particles to slower velocities due to different particle inertia. The calculations shown in Figure 2 for the 100 nm diameter particle predict a particle velocity at the lens exit of 216 (± 1) m s^{-1} and a particle transmission efficiency of 100%.

Additional calculations have been performed for a range of particle sizes (5 nm to 10 μm) to investigate both size-dependent particle velocities as well as particle focusing and transmission efficiencies through the lens. These results are presented in the section on particle collection efficiency and are compared to experimentally determined values.

Particle-Sizing Chamber

The focused particle beam exiting the lens is directed into the particle-sizing chamber through a 2 mm diameter skimmer cone (Beam Dynamics). The particle-sizing chamber is a flight tube maintained at $\sim 10^{-5}$ torr by a 550 L/s^{-1} turbo pump. The size-dependent particle velocities created by the gas expansion provide a means of obtaining the particle aerodynamic diameter by measuring particle TOF. The particle beam is modulated by a rotating wheel chopper in this chamber. Time-resolved detection of the particles, coupled with the known flight distance, gives the particle velocity from which the particle aerodynamic diameter is obtained.

The chopper wheel is 5 cm in diameter with two radial slits (0.13 cm wide, 180 degrees apart) giving a sampling duty cycle of 1.8%. The signal from an infrared photo-diode detector pair (monitoring the same slit that the beam passes through) defines the start of the particle TOF cycle and is used to synchronize time-resolved particle detection. The results presented here were performed in our prototype instrument, which has a particle flight distance of 39.7 cm measured from the chopper to the detector. The chopper operates at a fixed frequency, typically 150 Hz defining a TOF period of ~ 7 ms. Operation at faster speeds provides increased time resolution for the particle aerodynamic diameter measurement. The duty cycle of the chopper determines the aerosol throughput from the aerosol lens to the detector. The effective sampling rate is given by the product of this duty cycle and the flow through the lens tube (~ 100 sccm); thus, for 1.8% duty cycle, an aerosol volumetric flow of 1.8 sccm is sampled by the detector. The TOF measurement relies on a fast particle detection/vaporization scheme ($\ll 7$ ms TOF period), which also provides information on the composition of the aerosol.

Particle Detection Chamber

Detection is performed by directing the focused particle beam into a resistively heated closed-end tube. On collision, the volatile and semivolatile constituents in/on the particle flash vaporize. The vaporization source is integrally coupled to an electron impact ionizer mounted at the entrance of a quadrupole mass spectrometer. With the quadrupole tuned to a representative mass, bursts of ions are measured and, when sufficient particle mass is present, pulses from individual particles can be counted. Such single particle pulse widths are on the order of tens of microsecond time scale, much faster than the millisecond particle TOF time scale.

The particle-detection chamber is isolated from the particle-sizing chamber by a 4 mm diameter aperture. The detection chamber is differentially pumped by a 250 L/s^{-1} turbo molecular pump. The turbo pumps used on this apparatus are backed by a 60 L min^{-1} diaphragm pump that operates with ~ 1.2 torr inlet pressure. For some experiments a liquid nitrogen trap on the detection chamber was also used to reduce water vapor background levels in the mass spectrum.

Molecular ions are created in a custom built closed source electron impact ionizer/lens assembly designed to provide high electron emission current (up to 25 mA) and improved ion focusing and ion extraction into the quadrupole. This ionizer, which also integrates the particle vaporizer tube, is coupled to a UTI model 100 C quadrupole mass analyzer. Ions transmitted through the quadrupole are collected and amplified by an electron multiplier (Channeltron Model 4876). The output of the electron multiplier is terminated with a 24,000 ohm resistor so that an individual particle event can be resolved as a single pulse rather than many small pulses. The value of this resistor sets the electronic time resolution to ~ 30 μs, matched to the 6 μs sampling time of the data acquisition system discussed below.

The particle vaporizer is a small ceramic tube furnace with one end closed (0.3 cm ID opening by 1 cm length). The vaporizer is resistively heated by passing up to 5 watts of power through a 0.1 mm diameter coiled tungsten wire positioned inside the tube. The entrance of the vaporizer is mounted to the closed source ionizer lens element so that the vapor plume expands directly into the ionization region, a cylinder of ~ 1 cm^3 volume. As depicted in Figure 1, the vaporizer tube lies on the particle beam axis with the quadrupole mounted perpendicular to that axis.

The temperature of the vaporizer is monitored with a thermocouple mounted on the outside surface of the tube. The minimum vaporizer temperature is ~ 280°C, limited by radiative heating from the ionizer filaments. For results presented here, measured vaporization temperatures were 420°C for ammonium nitrate (NH_4NO_3), 320°C for dioctyl phthalate (DOP), and 600°C for polystyrene spheres (PSL). Operating at 600°C does not negate detection of either DOP or NH_4NO_3. The different temperatures used for each species should be viewed as limiting threshold temperatures for which efficient "flash" vaporization was observed. These initial studies suggest that higher temperatures provide more universal detection, though molecular decomposition for some species may increase at high vaporization temperatures. Detailed studies of the effects of vaporization temperature on the detection process needs to be investigated.

The high emission current closed source ionizer and tube furnace particle vaporizer improved particle detection compared to initial experiments which utilized a heated ribbon filament as both the particle vaporizer and the source of electron emission for vapor ionization. Since filament temperatures approaching 2000 K are required for electron emission, independent control of particle vaporization temperature was not possible. It was also observed that the flat vaporization surface resulted in poor signals for crystalline particles, likely due to particle bounce effects. The importance of vaporization filament geometry has been discussed by Sinha et al. (1982). The use of the higher performance closed ionizer and the coupling of the heater tube to it is one aspect of this instrument which differs from the earlier work by Allen and Gould (1981) and Sinha et al. (1982).

A mass spectrum illustrating detection of vaporized and ionized NH_4NO_3 aerosol is shown in Figure 3. This mass spectrum was obtained by scanning the quadrupole while

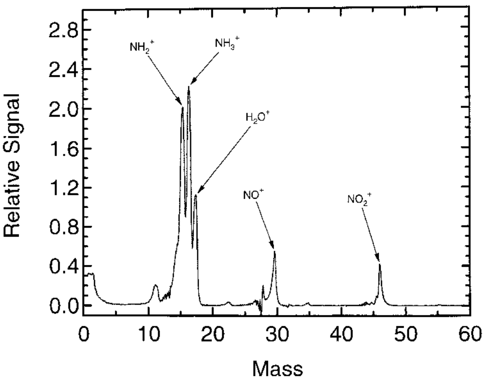

FIGURE 3. Mass spectrum of laboratory generated NH_4NO_3 particles showing detection of both the ammonium and nitrate components. This spectrum is a difference spectrum obtained by subtracting the spectrum measured with the particles off from the spectrum recorded with the particles on. HNO_3^+ and NO_3^+ ions are not observed. Particle vaporization temperature is 420°C and electron impact ionization energy is 70 eV.

continuously sampling moist aerosol at a relatively large aerosol mass loading (~ 100 μg m^{-3} or $\sim 2\times10^{-10}$ gm s^{-1} at the detector) with the particle beam chopper removed. The spectrum is included here for illustration purposes to show the nitric acid (NO^+ at m/z = 30, NO_2^+ at m/z = 46), ammonia (NH_2^+ at m/z = 16, NH_3^+ at m/z = 17), and water (H_2O^+ at m/z = 18) components. This mass spectrum is a difference spectrum obtained by subtracting background signals (recorded in the absence of the aerosol). The relatively low resolution in the water/ammonia region is limited by the subtraction process since these masses dominate background ion signals.

This mass spectrum illustrates an important feature of the detection process, namely, the separation of particle vaporization and ionization. Ammonium nitrate vaporizes into its volatile components, molecular ammonia and nitric acid vapors, which are identified by the ion fragmentation patterns as shown in Figure 3. The combination of efficiently separating vaporization from ionization and performing the ionization under controlled conditions as done here provides conditions which can maintain quantitative detection for multicomponent particles. The importance of separating the vaporization and ionization processes for aerosol analysis has recently noted by Morrical et al. (1998), who utilized a two-step laser desorption/ionization approach for analysis of individual organic particles followed by molecular TOF analysis. We have also observed molecular ion detection for each component of an internally mixed aerosol containing perylene, pyrene, and phenanthrene, again indicating that vaporization is separated from ionization. Previous work by Sinha et al. (1981), based on similar thermal particle vaporization and electron impact ionization techniques, demonstrated that matrix interference on the individual ion signal analysis is not important for a two component particle containing mixtures of glutaric acid and DOP.

A broad range of other aerosols has also been sampled and detected with this AMS, including bioaerosols (bovine serum albumin and bacillus subtilis), inorganic salts (NaCl, NaBr, NH_4Br, NH_4Cl, KCl, KI, $(NH_4)_2SO_4$ $(NH_4)_2CO_3$, $NaNO_3$), organics (benzoic acid, citraconic anhydride, oleic acid), and nicotine from cigarette smoke. Future work will investigate the ionization and detection efficiencies of more complex multicomponent aerosols.

The instrument is coupled to a data acquisition/analysis computer which sets the quadrupole mass, synchronizes the chopper timing and electron multiplier ion signals, and processes data in real time. In the current system, data acquisition is performed with 12 bit analog-to-digital conversion at 330 kHz, providing ~ 6 μs sampling time resolution of chopper and ion signals. For the results presented here on NH_4NO_3, the quadrupole filter was fixed to a specific mass setting (NO_2^+; m/z = 46). It is also possible to step-scan the quadrupole to pre-programmed mass settings or scan over a continuous range of masses. If operated in a mass stepping or scanning mode, the dwell time for a given mass must be an integer number of TOF periods. On changing the quadrupole setting, a settling time for the quadrupole electronics must be allowed, typically on the order of several milliseconds, or one TOF period. Integrating the ion signals over many TOF periods for each mass setting builds up statistical data for particle mass distributions. The sampling duty cycle for each ion mass depends on the number of programmed mass-to-charge settings and thus longer acquisition times are required since signals from the 1.8 sccm sampled aerosol flow is spread among multiple masses.

In parallel with the signal averaging for a given quadrupole setting, the fast digital signal processing allows every data point to be checked for the presence of a relatively large signal compared to the background. Such events result from vaporization of single particles which contain sufficient mass to generate signal pulses which are clearly distinguishable over background. Detection of such signals on-the-fly provides a direct particle counting mode as a function of particle TOF and quadrupole setting. As will be presented, the current sensitivity of this AMS for single particle counting with 100% efficiency is $\sim 2 \times 10^{-14}$ gm (~ 300 nm for a pure component particle) and the sensitivity for the signal averaging mode is ~ 0.25 μg m^{-3} for several minutes of signal integration. It should be noted that when data is collected by integrating over multiple TOF periods, composition data is averaged over the population of particles being sampled.

INSTRUMENT CALIBRATION AND TESTING

The performance of the AMS has been tested using a calibrated monodisperse aerosol produced with a differential mobility analyzer (TSI model DMA 3071). Particles were generated with an atomizer (TSI model 3076) followed by a diffusion dryer. The monodisperse output of the DMA (or the atomized polydisperse aerosol) was passed into a 2.2×80 cm Pyrex glass flow tube where aerosol concentration could be diluted by addition of dry/filtered nitrogen gas. A fraction of the aerosol was sampled near the exit of the aerosol flow tube by both the AMS and a condensation particle counter (TSI model CPC 3010). The majority of the flow tube effluent was vented. This aerosol generation system was used to calibrate the particle size-dependent TOF measurement to determine the particle collection/detection efficiency of the AMS and to allow comparison to total size resolved mass and number density measurements.

Aerodynamic Particle Sizing by Particle TOF Measurement

Particle TOF spectra for NH_4NO_3 particles presized by the DMA are shown in Figure 4 for six different DMA mobility settings. For these measurements the quadrupole filter was set to $m/z = 46$ to measure the NO_2^+ ion intensity. The negative signal intensity shown in the plots is a measure of the electron current emerging from the electron multiplier and is proportional to the NO_2^+ ion density formed from electron impact ionization of the vaporized NH_4NO_3 particles. Each TOF spectrum represents 1–3 min of data collection and averages ~ 5 to 10,000 individual particle vaporization events (varying inversely with particle size). The structure in the spectra shows both the time response to the singly charged particles of the stated mobility diameter and the multiply charged particles of larger diameter which are simultaneously sized by the DMA since they have the same electrical mobility. The mass weighted detection process allows the multiply charged/larger diameter DMA particles to be clearly resolved even though they are present in small fractions. During the course of this work we found that the addition of a second aerosol neutralizer (in series with the ^{85}Kr(β) charger which is the standard charger in the TSI DMA, Model 3077) was required to match equilibrium particle charging/neutralization predicted by the Boltzmann law (Liu and Pui 1974). If only the TSI charger were used, too many particles carried a charge in excess of three charge units. The additional charger used was a ^{210}Po(α) charger (NRD, Model P-2031, 20 mCi) and was placed at

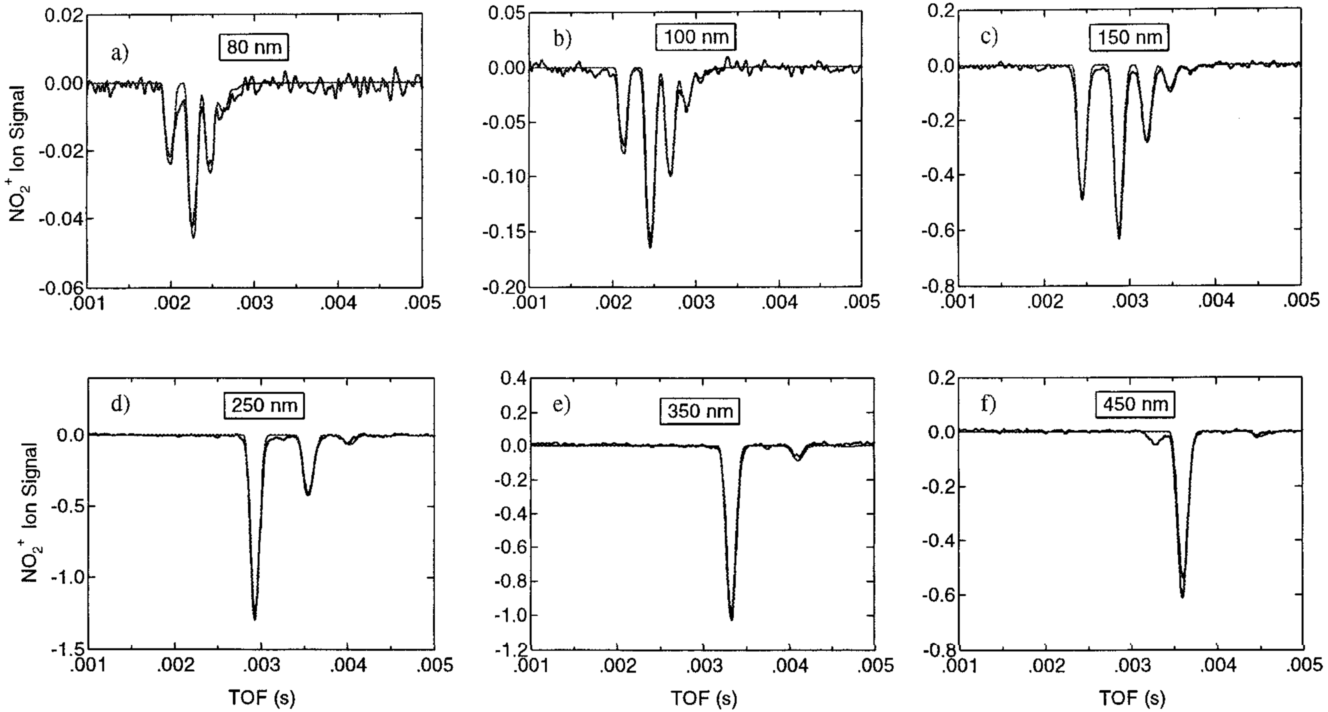

Figure 4. Particle TOF spectra for NH_4NO_3 particles presized by the DMA. Negative signal intensity is a measure of the vaporized NH_4NO_3 particle mass detected as the NO_2^+ ion (m/ z =46). Larger diameter particles of equivalent electrical mobility (multiply charged particles) are clearly resolved. The particle mobility diameter listed in each panel is for the singly charged particle. The thin smooth line models the performance of the AMS measurement. See text for details.

the inlet to the DMA, upstream of the ^{85}Kr charger.

The solid lines in Figure 4 model the performance of the AMS, taking into account the polydisperse aerosol distribution, the transfer function of the DMA (including Boltzmann equilibrium aerosol charging levels), the transfer function of the AMS, the linear mass-weighted AMS detection scheme, and the AMS particle collection efficiency. The DMA transfer function used here is the triangular function derived from DMA gas flow rates (Knutson and Whitby 1975). For these measurements the DMA flows were $q_c = q_m = 5.92$ SLPM and $q_s = 0.51$ SLPM, where q_c is the clean air flow, q_m is the main outlet flow and q_s is the sample flow (Knutson and Whitby 1975). The polydisperse aerosol distribution was represented by a log-normal distribution function (Fuchs 1989) determined from a fit to the inverted DMA-CPC data measured in parallel with the AMS data plotted in the figure (see later discussion on Comparison to DMA and Figures 12a and 13a). The transfer function for the AMS (also discussed in a later section) takes into account the time width of the "open gate" associated with the particle beam chopper and the finite-time profile of a single particle vaporization event. For these measurements the chopper was operated at 155 Hz.

The model prediction assumes complete particle vaporization with molecular ionization and detection linearly proportional to volatile particle mass with ionization efficiency determined directly from single particle observations. Particle collection efficiency was independently measured to be 100% for all the data sets shown in Figure 4, with the exception of the 450 nm data in panel *f*. Further discussion of both ionization efficiency and particle transmission/collection efficiency is presented in the next section. The series of measurements shown in Figure 4 is summarized in Table 1 which lists, for each peak, signal averaging time, mobility diameter, aerodynamic diameter, particle velocity, and the number and mass concentration from the model prediction. Mass loadings as low as 0.25 μg m^{-3} are observable for the 80 nm mobility diameter data (e.g., $q = 4$) with a signal to noise of about 1:1.

The variation in particle TOF with particle size, as seen in Figure 4, is a direct measure of the size-dependent particle velocities resulting from the controlled aerosol expansion into vacuum. Particle velocity is determined by the ratio of the flight distance to the measured TOF at the peak of the ion signal intensity. Particle velocity measurements such as those shown in Figure 4 have been performed for DOP and calibrated PSL spheres (Duke Scientific Corp.). We note here that the measurements made with the PSL spheres also served as a check on the performance of the DMA as a calibrated aerosol source.

The results of the aerodynamic particle velocity measurements are plotted in Figure 5 as a function of aerodynamic diameter. For spherical particles, aerodynamic diameter is simply defined as the product of the geometric diameter and the particle density. In this system, where the aerosol expands into the free molecular regime, the particle velocities are expected to scale by the aerodynamic diameter with an inverse power dependence. Values for the particle density used here are 0.91, 1.05, and 1.72 gm cm^{-3} for DOP, PSL, and NH_4NO_3. Since we are calibrating using particle mobility diameter (sized by the DMA), one needs to consider the relation between mobility diameter and geometric diameter. For both DOP and PSL, which are spheres, the mobility diameter is equal to the geometric diameter. For nonspherical, crystalline NH_4NO_3 particles, however, the effect of particle shape needs to be considered in defining an aerodynamic diameter (Zie-

TABLE 1. Summary of TOF data shown in Figure 4.

						Model Integrated	
Figure 4 Panel id.	Signal Integration Time, sec	Particle Charge	Mobility Diameter (nm)	Arerodynamic Diameter	Particle Velocity (m/s)	Particle Density (#/cc)	Particle Mass (ug/m3)
a	180	1	80	110	200.5	1331	0.64
		2	119	164	176.2	787	1.26
		3	152	209	162.1	222	0.76
		4	183	252	151.8	42	0.25
		5	213	293	143.8	6	0.05
b	180	1	100	138	186.6	2335	2.18
		2	151	208	162.4	1369	4.50
		3	196	270	148.2	392	2.79
		4	238	327	138.1	82	1.05
		5	279	384	130.2	14	0.29
c	180	1	150	206	162.8	4180	13.24
		2	235	323	138.7	1429	17.39
		3	314	432	124.6	292	8.38
		4	389	535	114.8	52	2.86
		5	463	637	107.3	9	0.85
d	60	1	250	344	135.6	2587	37.26
		2	415	571	112.0	221	14.51
		3	573	788	98.7	18	0.61
e	60	1	350	482	119.6	793	31.20
		2	602	828	96.7	21	4.11
f	60	1	450	619	108.5	257	19.32
		2	793	1091	86.6	3	1.16

mann et al. 1995). To obtain the best fit of the NH_4NO_3 particle velocity data in Figure 5 a shape factor of 0.80 was used. This shape factor is actually the product of the shape factor relating mobility and geometric diameter from the DMA measurement and the shape factor relating aerodynamic and geometric diameter from the AMS measurement.

The dotted line in Figure 5 is the result from the FLUENT model calculation for spheres with a density of 1 gm cm^{-3}. The agreement between the model and data is very good. For larger particles, the relation between diameter and velocity is described by a simple power law. For smaller particles, velocities deviate from the power law as particle velocities approach the limiting molecular velocity of the gas expansion. The solid line in the figure is best fit to the expression,

$$v = \frac{v_g}{1 + (D_{aero}/D^*)^b},$$

where D^* and b are fitted coefficients ($D^* = 27.2 \pm 0.5$ nm and $b = 0.479 \pm .004$), D_{aero} is the aerodynamic diameter (nm), and v is the particle velocity (m s^{-1}). In the limit of zero particle diameter, particle velocity extrapolates to $v_g = 592$ m s^{-1}, the velocity of the molecules on the center-line of the exit of the aerodynamic lens as predicted by FLUENT. Here, D^* is the characteristic particle diameter for acceleration in the expansion from the aerodynamic lens.

Single Particle Counting

The particle TOF measurement relies on a fast particle mass detection scheme. For

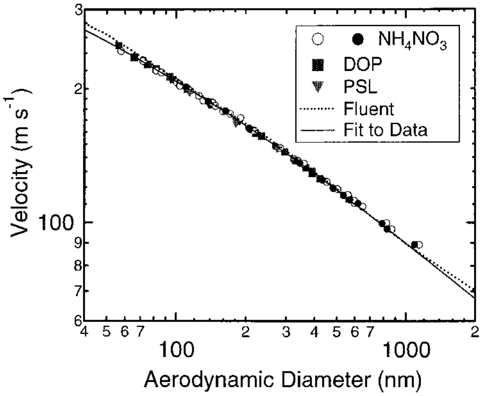

FIGURE 5. Particle velocity plotted as a function of particle aerodynamic diameter. All data points are from particle TOF measurements using the DMA as a source of calibrated particles. The solid circles are from the TOF data shown in Figure 4. The dashed line is the prediction from the FLUENT calculations. The solid line is a fit to the data (see text).

particles composed of (or containing) volatile and/or semivolatile species, the time scale for particle flash vaporization, ionization, and quadrupole detection is rapid compared to the millisecond TOF time scale. For particles containing sufficient mass, individual particle vaporization events can be clearly time-resolved as bursts of ions by monitoring the output of the quadrupole mass filter tuned to a representative mass. This aspect of the data collection system is conceptually similar to a pulse counting signal processing system, where in this case the discrimination is set by the software such that background (i.e., nonparticle) ion pulses emerging from the electron multiplier are not counted since they do not exceed the threshold intensity which discriminates between particle and nonparticle pulses. If a signals pulse exceeds a threshold value, the data collection software counts this as a discrete particle vaporization event. This data is stored separately from the integrated signals (such as shown in Figure 4). For particles that generate ion signals which are only slightly larger (or smaller) than the individual particle discrimination level, single particle detection/counting is subject to statistical variability and as a result the efficiency of direct particle counting decreases with the number of molecules in the particle. For cases where a particle does not contain enough molecules to generate clearly distinguishable individual particle pulses, averaging the output of the quadrupole ion signal over multiple TOF periods still give rise to measurable TOF spectra, allowing particle size to still be accurately determined.

Time-resolved detection of pure NH_4NO_3 particles presized by the DMA is shown in Figure 6. Each curve represents an average of about 100 individual particles which have been detected above the threshold (dashed line in the figure). The variation of the pulse height is linear with size for 200, 320, and 440 nm DMA selected particles. The error bars (standard deviation of the sample for the total ions in each pulse) correlate well with the expected statistical variability for the finite number of ion counts. The peak in signal intensity for each trace has been centered at $t = 0$ for comparison purposes. The width of the average single particle pulse is narrow, ~ 30 μs at the half width, and is independent of particle size over the range investigated here. The particle signals are electronically broadened by adjusting the response time of the detection electronics to match the 6 μs sampling rate of the current data acquisition system.

The smallest signal in Figure 6 represents single ion pulses originating from the background at m/z = 46 in the mass spectrometer. This average single ion signal is obtained by reducing the threshold discrimination level and counting and storing individual ion signals for a reduced emission

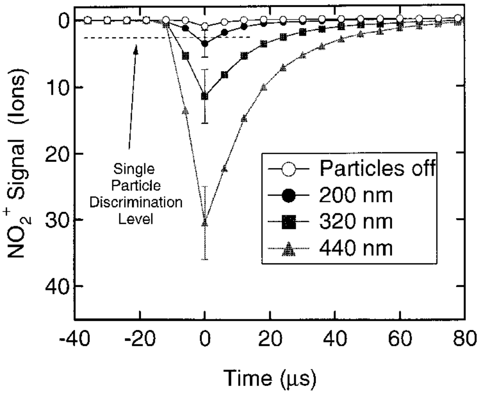

FIGURE 6. Average of NH_4NO_3 individual particle pulses. These particles were pre-sized by the DMA which was set to deliver particles of mobility diameter of 200 nm ($q = 1$). The multiply charged particles of larger diameter are also observed, 320 nm ($q = 2$) and 440 nm ($q = 3$). The signal axis is a measure of the number of NO_2^+ ions produced by electron impact ionization of the flash-vaporized incident particle which exceeds the single particle discrimination level (dashed line) set by the data collection software. Approximately 100 single particles events were counted and averaged for display. The data points represent the 6 μs sampling rate of the data acquisition system. Each particle size is actually detected at different time-of-flights but they have been re-plotted with the peak intensities arbitrarily shifted to $t = 0$ to illustrate relative signal intensity and particle widths. In the absence of any particles, an ion signal is observed (open circles) which originates from the molecular background present at this mass setting. Error bars represent the standard deviation of the sample for the total ions in the pulse.

current setting in the electron impact ionizer (i.e., low ion count rates). The integrated area under the single ion pulses measures the charge in Coulombs emerging from the electron multiplier and provides a normalization factor allowing the area under each of the average particle signals to be converted to the number of ions detected per incident particle.

Analysis of particle pulses detected for pure component particles has demonstrated that the detection scheme is linear with the volatile mass of the particle. In other words, the number of ions detected per incident particle varies linearly with the number of volatile molecules of a specific type in the particle. Results of individual particle detection experiments are summarized in Figure 7, which plots the number of ions detected per incident particle as a function of the number of molecules per particle for pure component NH_4NO_3 and DOP particles. The 1:1 correlation between the number of ion-per-particle and the number of molecules-per-particle (shown as the dashed lines in the figure) demonstrates that these particles fully vaporize and are detected linearly with their mass. The error bars in the figure are the standard deviation of the mean for both the ions detected per particle and for the deviation in the number of molecules per particle resulting from "binning" the data.

Linear fits to the data shown in Figure 7 yield ionization efficiencies of 1×10^{-6} ions

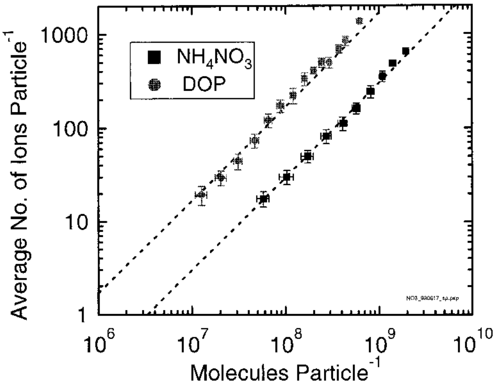

FIGURE 7. Average number of ions detected by the quadrupole mass spectrometer per incident particle varies linearly with the number of molecules in the particle. Linear regression to this data provides a measure of the effective ionization efficiency for each species (see text). The quadrupole was set at m/z = 56 and m/z = 46 for DOP and NH_4NO_3 respectively. Vertical error bars are the standard deviation from the mean ions molecule^{-1} value and the horizontal error bars are the standard deviation of the mean number of molecules in the particle (see text).

molecule^{-1} for DOP and 2×10^{-7} ions molecule^{-1} for NH_4NO_3. These values for the ionization efficiency are two to three orders of magnitude lower than what can be expected for a high efficiency electron impact ionization source. Part of the reason for this low value is that we are plotting only one of several ion peaks. A complete analysis would sum all ion signals observed for a given species. The low efficiency is also believed to be due in part to nonoptimal overlap of the particle vapor plume with the electron density in the ionizer as well as overall ionizer/quadrupole performance. Improving ionization efficiency will improve instrument sensitivity and allow counting of smaller individual particles. This is an area of active investigation and significant improvements are anticipated.

Figure 7 also illustrates the current single particle counting limits. In order to clearly resolve a particle vaporization event from the background, the particle must generate an ion signal larger than approximately 20 ions particle^{-1} to be detected and counted as an individual particle. For a pure NH_4NO_3 particle this currently corresponds to $\sim 5 \times 10^7$ molecules, $\sim 7 \times 10^{-15}$ gm, or a diameter of $\sim$ 200 nm. For a particle of this size/mass the counting efficiency is not 100% due to the statistical variability of the signal and the simple threshold discrimination used. Developing more sophisticated particle detection algorithms, improving ionization efficiency, and reducing background will lead to improved individual particle detection limits. For pure NH_4NO_3 particles, counting efficiency reaches 100% for particles $> \sim$ 300 nm in diameter (i.e., particles containing $> \sim 2 \times 10^8$ molecules or $> \sim 2 \times 10^{-14}$ g mass). Particle counting efficiency depends on ionization efficiency and ion fragmentation patterns and will vary somewhat from species to species.

Particle Collection Efficiency

Experiments were performed to determine the AMS particle collection efficiency as a function of particle size, using the DMA and CPC as a calibrated aerosol source. Monodisperse aerosol output of the DMA was directed into the aerosol flow tube from which both the AMS and the CPC drew samples. Aerosol concentration in the flow tube was varied via dilution with added dry/filtered nitrogen gas flow. Results of these experiments are shown in Figure 8, which plots the particle number density measured by the AMS versus the number density measured by the CPC for different aerosol concentrations. The number density measured by the AMS is obtained from the direct single particle count rates (described above) and converted to a number density by dividing by the effective gas sampling rate (1.8 cm^3 min^{-1}). The measurements were performed for NH_4NO_3 particles at four different sizes: 350, 450, 550, and 700 nm. A linear fit to each data set in Figure 8 yields the collection efficiency for

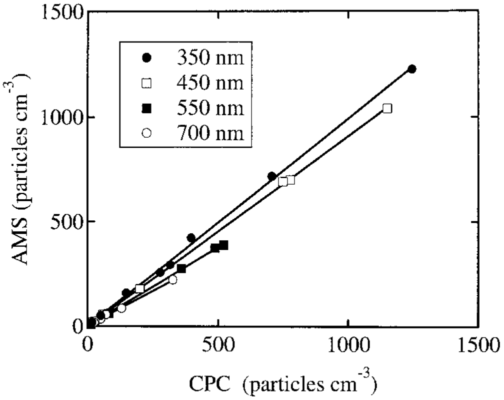

FIGURE 8. Comparison of particle number density as measured by the AMS and as measured by the CPC for four different size NH_4NO_3 particles. The slope from a linear fit to each data set data yields the AMS particle collection/detection efficiency and is 0.99, 0.91, 0.76, and 0.68 for the 350, 450, 550, and 700 nm mobility diameter particle, respectively.

that particle size. The collection efficiencies are 0.99, 0.91, 0.76, and 0.68 for the 350, 450, 550, and 700 nm diameter particles, respectively.

This direct comparison of count rates between the AMS and the CPC could be performed only for the relatively large DMA particles which are extracted from the tail end of the polydisperse aerosol distribution and which can be directly counted as single particles with 100% efficiency. For particles smaller than about 300 nm, the effect of multiply charged larger diameter particles of equivalent mobility which are simultaneously sized by the DMA and also counted by the CPC need to be accounted for. For these smaller particles, the collection efficiencies were obtained from the ratio of the area of the TOF data to the model prediction, as shown in Figure 4. Recall that the model is the log-normal distribution function that was obtained from the fit to the inverted DMA-CPC data which will be discussed later (Figure 12a). Even though direct single particle counting efficiency drops off for particles below ~ 300 nm for the pure NH_4NO_3 particles investigated, the total particle mass is still accurately obtained by signal averaging as is shown by the match of the solid lines to the particle TOF data in Figure 4.

The AMS particle collection efficiency measurements are summarized in Figure 9. The circles represent the collection efficiency measurements from particle counting (slope of the lines from Figure 8) and the squares are obtained from the ratio of the area of the TOF data to the area of the DMA-CPC prediction shown in Figure 4 (for the $q = 1$ peak only). The solid line in Figure 9 is the prediction based on the FLUENT calculations. The decrease in collection efficiency for the larger diameter particles is due to impaction losses at the entrance to the aerodynamic lens and is well represented by the data. The more dramatic decrease in collection efficiency for the smaller diameter particles (< 70 nm) results from less efficient focusing in the aerodynamic lens. Although these particles are transmitted through the lens, their angular dispersion upon exiting the lens is larger than the 0.07 radian required to pass through the 3 mm opening to the particle vaporizer over the 45 cm total particle flight path.

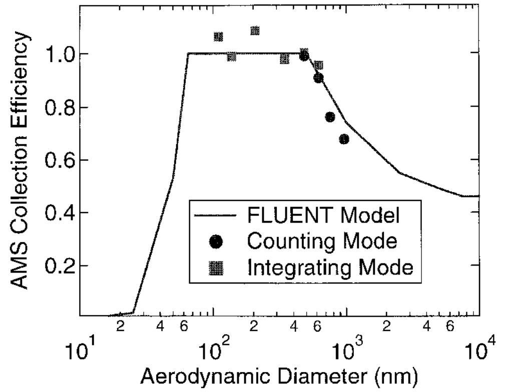

FIGURE 9. Summary of the AMS particle collection/detection efficiency as a function of aerodynamic diameter. Solid line is FLUENT model prediction. Circles are efficiencies determined by comparing AMS and CPC counting rates (data from Figure 8). Squares are collection efficiencies determined from the ratio of the measured to the calculated integrated area of the TOF data shown in Figure 4 (note that the data points originating from Figures 4 and 8 have been converted from mobility to aerodynamic diameter using particle density of 1.72 and a shape factor of 0.8).

AMS Transfer Function

The time width of the open gate of the TOF chopper limits the resolution of the particle TOF measurement. The spread of mass across the TOF space is a function of the speed of the chopper and the chopper slit widths. Likewise, the finite width of individual particle vaporization events also broadens the true mass distribution in time. These effects are illustrated in Figure 10,

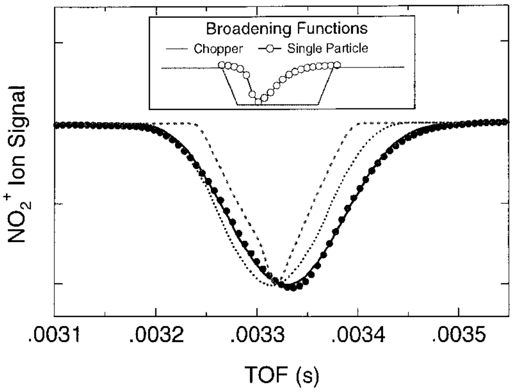

FIGURE 10. Broadening effect of the finite width of the particle beam chopper and the single particle vaporization width on the AMS TOF measurements for 350 nm mobility diameter particles. Dashed line is the volume weighted output of DMA. Dotted line illustrates the broadening effect of the chopper on the DMA output. Solid line models the broadening effect of both the chopper and the single particle on the DMA output. Circles are an expanded portion of the same TOF data shown in Figure 4.

which expands the AMS TOF observations of a DMA-selected 350 nm particle (data from panel e in Figure 4). The AMS broadening functions are shown in the upper portion of Figure 10 scaled to the TOF time axis. The solid line is the chopper function whose width of 0.12 ms is calculated from the chopper duty cycle (1.8%) and the frequency (155 Hz). The open circles represent the single particle broadening function measured directly from NH_4NO_3 particle events. The effect of these functions on the particle TOF measurement is shown in the lower portion of the figure. The dashed line is the modeled output from the DMA, mass weighted and converted to TOF space (and normalized for presentation purposes), corresponding to a size resolution of ~ 12 (for DMA flows noted above). The dotted line shows the effect of passing the chopper function through the DMA prediction. The solid line includes both the chopper and the single particle broadening functions. The convolution of DMA and AMS transfer functions quantitatively and accurately predict the measured TOF data.

The complete model (the solid line) slightly shifts the predicted signal to longer observed TOF times due to the single particle broadening function. This shift of ~ 20 μs has been taken into account in analyzing the velocity data shown in Figure 5. Recall that the width of individual particle events is broadened by the detection electronics to match the 6 μs sampling rate of the data acquisition system.

Figures 4, 5, and 10 indicate that the resolution of the aerodynamic particle size measurement is very high. This implies that the distribution of particle velocities generated by the particle beam forming lens is sharply peaked for a given particle diameter. The validity of the model fits was investigated by varying both DMA (i.e., q_c/q_s flows) and chopper (i.e., chopper speed) resolution functions and quantitatively observing changes in the AMS TOF resolution. Current measurements indicate that the resolution of the AMS is not limiting for DMA resolution up to 20. At this point the ultimate resolution of the AMS has not been determined but it is likely limited by the finite width of the individual particle pulses and the chopper width rather than the particle velocities generated by the aerodynamic lens. Operational size resolution of the AMS TOF instrument will involve optimization of the trade off between chopper open gate time and sampling duty cycle.

Particle Beam Width Measurements

A series of experiments was performed to measure the width of the particle beam by translating a 75 μm wire across the particle beam and measuring beam attenuation as a function of wire position. Transmission of the particles through the inlet to the detector was calculated from the ratio of particle count rates measured by the mass spectrometer and count rates measured by the CPC. Beam transmission is plotted in Figure 11 for DOP (solid circles) and NH_4NO_3 (open circles) as a function of wire position (set with a micrometer translator). It can be seen from the data that the particle beam is narrow ($<$ 1 mm diameter) and that the width of the DOP particle beam is narrower than that of NH_4NO_3 particles. The lines in the figure represent best fits to the data points obtained by inverting the data and fitting them to an assumed Gaussian distribution with only the width as the fitted parameter. The width (FWHM) of the fitted distribution is 0.13 mm for the DOP data set and 0.23 mm for the NH_4NO_3 data set. The wire assembly intersected the particle beam 16 cm downstream of the aerodynamic lens, about 1/3 of the total distance from the lens exit aperture to the particle vaporizer. Beam widths at the detector are estimated to be three times larger, assuming that the particle beam originates as a point source at the lens exit (see Figure 2).

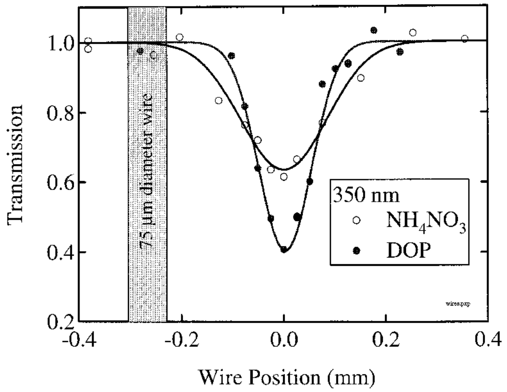

FIGURE 11. Particle beam width measurement for spherical DOP and nonspherical NH_4NO_3 particles. Beam widths are determined by passing a 75 µm diameter wire across the particle beam path and calculating particle transmission from the ratio of the single particle count rates measured by the mass spectrometer to the count rates measured by the CPC. Beam broadening is observed for nonspherical particles. The solid lines represent a Gaussian fit to the inverted data yielding FWHM values of 0.13 mm for DOP and 0.23 mm for NH_4NO_3.

The results of these measurements suggest that the width of the particle beam varies with particle morphology. The larger beam width observed for NH_4NO_3 is consistent with the fact that a shape factor was derived for NH_4NO_3 particles from the size dependent velocity measurements. Reduced particle focusing for nonspherical particles by the aerodynamic lens has been discussed by Liu et al. (1995b) and experimentally observed by Ziemann et al. (1995) and by Schreiner et al. (1998). Beam broadening is due to nonsymmetric lift forces encountered during particle focusing and acceleration. The beam width measurements and the FLUENT calculations, which also provide information on beam divergence angles, can be used to guide the design of aerosol sampling systems with optimized performance for a particular application. For example, the collection aperture on the particle vaporizer can be enlarged and the total flight path can be shortened to optimize collection of smaller particles in the vaporizer.

Comparison to DMA Distribution Measurement

An experiment was performed to quantitatively compare the measurement of the same NH_4NO_3 polydisperse aerosol distribution obtained by the AMS and by the DMA-CPC. The NH_4NO_3 aerosol was atomized, dried in a diffusion drier and then analyzed separately with the DMA and AMS. The DMA was operated in the step-scanning mode using the CPC to measure the particle number density, as shown in Figure 12a, which plots the CPC particle number density versus the DMA voltage setting. The polydisperse aerosol flow was then removed from the DMA input and the flow was measured with a soap film bubble meter and directed into the aerosol flow tube. An additional dilution flow of dry air (of a known amount) was added to the flow tube so that the total aerosol concentration could be measured accurately by the CPC3010. The time resolved data from the AMS measurement of the same polydisperse NH_4NO_3 aerosol (at a lower aerosol concentration) are shown in Figure 12b, which plots the NO_2^+ ion signal intensity as a function of particle TOF. Note that the DMA-CPC measurement is an aerosol number density measurement and that the AMS is an aerosol mass measurement.

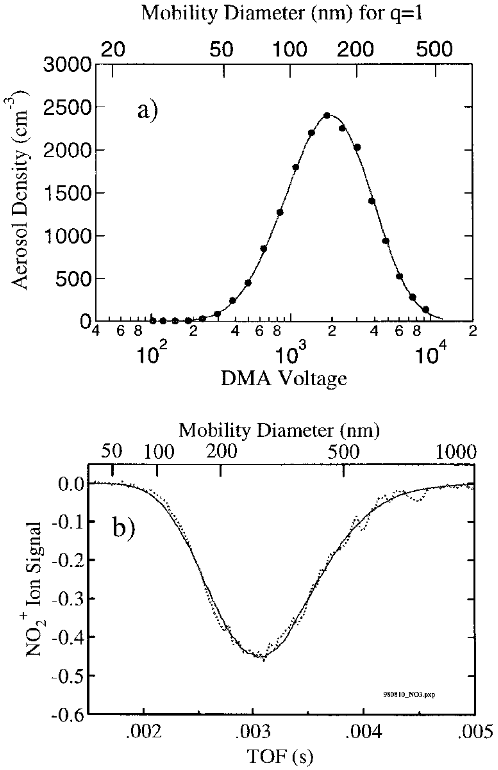

FIGURE 12. (a) Raw data for DMA-CPC measured NH_4NO_3 polydisperse distribution. (b) Raw data for the same NH_4NO_3 polydisperse aerosol as measured by the AMS.

Both sets of data were inverted and fit to a log-normal distribution function of the same form, shown by the solid lines in each panel of Figure 12. The data inversion process for the DMA was performed using an algorithm which makes an initial guess at the log-normal distribution, passes that distribution through the DMA transfer function (Knutson and Whitby 1975), compares the integrated modeled counts to the raw data, then makes a new guess at the log-normal distribution. The three coefficients which describe the log-normal distribution (the total number, the width, and the mean diameter) are optimized using the Marquardt nonlinear least squares fitting method (see Press et al. 1988). The inversion process for the AMS uses the transfer function described previously, the particle TOF-diameter relationship, the collection efficiency, and the NO_2^+ ion signal/particle mass relationship, all of which have been determined in this work. Similarly, for the AMS measurement, the inverted data are fitted to an assumed log-normal distribution using the same nonlinear fitting routine.

The results of the data inversion for both the AMS (solid curve) and the DMA-CPC (dashed curve) are compared in Figure 13, which plots the particle distributions as a function of mobility diameter. Figure 13a plots number density distribution, N/dln(Dp). The two distributions agree well in both absolute intensity and width.

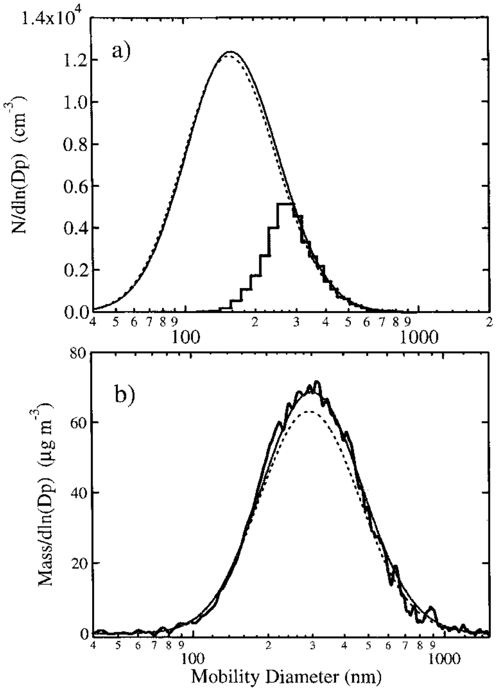

FIGURE 13. Quantitative comparison of the aerosol number density distribution (a) and the mass distribution (b) measured by the AMS (solid lines) and by the DMA-CPC (dashed lines). The lines are log-normal distribution functions from the fits to the inverted raw data (Figure 12). The histogram shown in (a) is the particle number density determined from particle counting measured by the AMS while sampling the same aerosol. The apparent disagreement in the small size range ($<$ 300 nm) is due to decreased single particle counting/detection efficiency (see text for details). The complete mass distribution, however, is accurately measured by integrating over many TOF periods as is shown by the data (jagged line) in (b).

The total particle number density of 14,210 particle cm^{-3} obtained from the log-normal fit to the AMS data agrees within 2% to the CPC measured count of 13,940 particles cm^{-3} (corrected for coincidence counting from the displayed count rate of 12,800 particles cm^{-3}). Also shown in this figure is a histogram of the counted AMS particle data that was simultaneously processed by the data acquisition software during acquisition of the averaged signal shown in Figure 12b. For NH_4NO_3 particles larger than ~ 300 nm diameter, the histogram plot and the log-normal distribution overlap. For particles smaller than 300 nm, the single particle detection/counting efficiency drops off as individual particle events are not clearly discriminated from the background signal.

Although individual particles smaller than ~ 300 nm are not counted with 100% efficiency, the overall aerosol mass distribution is accurately measured by integrating the AMS signal over many TOF periods (approximately 3 min). This is shown in Figure 13b, which plots the same log-normal functions from Figure 13a as mass weighted distributions, mass/dln(Dp), together with the AMS data (the thick solid curve). The agreement of the distributions again is very good. The total mass from the fitted AMS distribution (solid line) is 79 μg m^{-3}, slightly larger than the 72 μg m^{-3} derived from the DMA-CPC number density distribution (dashed). This difference in the mass distribution may be indicative of slight changes in the polydisperse distribution when bypassing or passing through the DMA.

SUMMARY/DISCUSSION

For aerosols containing volatile and semivolatile species, this aerosol mass spectrometer has the capability to provide quantitative information on particle size distributions as a function of chemical composition (quadrupole mass setting) in real time. The instrument uses an aerodynamic particle beam forming inlet to efficiently and quantitatively deliver aerosol into vacuum. Aerodynamic particle diameter is determined by measuring particle velocity via TOF. Fast particle detection is achieved via flash vaporization of volatile and semivolatile components of the particle in a resistively heated tube. The resulting vapor is ionized by electron impaction and positive ions are detected using a quadrupole mass spectrometer.

The theoretical performance of the aerodynamic inlet as predicted by the FLUENT model has been verified experimentally. Collection efficiency of the particles at the detector approaches 100% for particles of aerodynamic diameters in the range of 70 to 500 nm. The predicted particle velocity created by the expanding gas very closely matches the experimental measurements. Particle beam widths formed by the inlet vary with both particle size and shape. Spherical particles are focused more efficiently than nonspherical particles and larger particles are focused better than smaller particles. For 350 nm diameter DOP and NH_4NO_3 particles, the measured beam width at the point of detection is < 1 mm in diameter.

The detection process has been shown to be linear in particle mass for the pure component particles investigated here and to have fast time response (of order 10^{-5} s), allowing individual particles with sufficient mass ($> \sim 2 \times 10^{-14}$ gm) to be directly detected and counted with 100% efficiency as a function of aerodynamic diameter. Particles containing less mass can be detected by averaging quadrupole mass spectrometer ion signals over many TOF periods providing detection limits for particle mass $> 0.25\ \mu g\ m^{-3}$ for several minute integration times. These detection limits are based on the results presented here for the pure NH_4NO_3 particles. Size resolved aerosol mass distributions measured by the AMS for pure component submicron NH_4NO_3 aerosol agree very well with that measured using a DMA-CPC. A factor of 10 to 100 improvement in the ultimate sensitivity of the AMS is expected based on improvements in the mass spectrometer performance and in differential pumping to reduce vapor background levels.

There are several key factors which will govern the overall utility of this AMS for measuring size-resolved mass distributions, the most important of which is that the species must first vaporize to be detected. Given this initial condition, there are other important issues. For example, the quantitative results for pure component particles presented here must be extended to detection of mass fractions within multicomponent particles. Separating the particle vaporization process from the ionization process is an important concept in this regard. For species which efficiently vaporize, this detection process should provide the same quantitative results that are obtained by conventional electron impact ionization mass spectrometry of multicomponent gas phase mixtures. Finally, as with all mass spectrometric approaches, interpretation of a mass spectra for an unknown sample can be complicated by mass interference problems. This issue is most relevant regarding its use as a field instrument. However, if the detection process is quantitative (linear with mass), size resolved aerosol mass loading as a function of detected ion mass will provide useful chemical information.

This AMS should be applicable to both laboratory and field measurements. In its current state, it will be used as a diagnostic for a wide range of aerosol kinetics studies by coupling it to an aerosol flow reactor. The design features of the AMS can also be incorporated into a relatively small portable device which could find utility as a field instrument to provide information on size-resolved mass distributions for ensembles of particles. For this application, the quadrupole can be programmed to scan the entire mass spectrum, to sample a few selected masses or to monitor some combination of both. For example, one approach would monitor water, ammonia, nitrate, and sulfate mass peaks every second while also scanning many other mass peaks with lower duty cycle. Measurement of mass loading as a function of aerodynamic diameter would provide data similar to that obtained by impactor sampling, but on a much faster time scale (tens of minutes) with real-time analysis, rather than tens of hours with extensive post-analysis.

Based on the measured detection limit of 0.25 μg m^{-3} (corresponding to 3 min averaging for one quadrupole setting and a pure component particle) one can estimate the minimum concentration of ambient aerosol, which will provide a measurable signal over this time scale as a function of particle diameter. For 70, 100, and 500 nm diameter particles, number densities of 1000, 300, and 2 particles cm^{-3} can yield measurable signals. These estimates are based on single component particles of unit density. Sensitivity is expected to scale proportionately with the volume fraction of volatile or semivolatile components in the particle and acquisition times will scale inversely with the number of quadrupole settings. The range of aerosol components for which this will be true remains to be demonstrated through both laboratory and field testing.

Particle composition information would be limited to size-resolved analysis of particle ensembles since the quadrupole mass spectrometer can sample only one mass for each particle. We note that the use of a molecular TOF mass spectrometer, coupled with the quadrupole, would enhance the analytical power for sampling unknown particles. At somewhat reduced sensitivity, this would allow an entire mass spectrum to be obtained for a single particle. Trade-offs in size, power, and data analysis requirements remain to be assessed for a particular sampling scenario. Field instrument design issues are currently being addressed.

This work was supported by the National Science Foundation, the U.S. Environmental Protection Agency, and the Office of Naval Research. We would like to thank Paul Ziemann and Peter McMurry for sharing with us the design of the aerosol sampling inlet and for their assistance during the early stages of this work. We would also like to thank Anthony Strawa for providing the calibrated wires and for his assistance during the particle beam width measurements and Richard Flagan for helpful discussions regarding the operation of the DMA.

References

Allen, J., and Gould, R. K. (1981). Mass Spectrometric Analyzer for Individual Aerosol Particles, *Rev. Sci. Instrum.* 52:804–809.

Carson, P. G., Neubauer, K. R., Johnston, M. V., and Wexler, A. S. (1995). On-Line Chemical Analysis of Aerosols by Rapid Single-Particle Mass Spectrometry, *J. Aerosol Sci.* 26:535–545.

Eichler, T., de Juan, L., and de la Mora, J. F. (1998). Improvement of the Resolution of TSI's 3071 DMA via Redesigned Sheath Air and Aerosol Inlets, *Aerosol Sci. Technol.* 29:39–49.

FLUENT (1995). Version 4.47, Fluent Inc., Lebanon, New Hampshire.

Fuchs, N. A., (1989). *The Mechanics of Aerosols*, Dover Publications, Inc., New York, p. 12.

Gard, E., Mayer, J. E., Morrical, B. D., Dienes, T., Fergenson, D. P., Prather, K. A. (1997). Real-Time Analysis of Individual Atmospheric Aerosol Particles: Design and Performance of a Portable ATOFMS, *Anal. Chem.* 69:4083–4091.

Gieray, R. A., Reilly, P. T. A., Yang, M., Whitten, W. B., and Rasey, J. M. (1998). Tandem Mass Spectrometry of Uranium and Uranium Oxides in Airborne Particulates, *Anal. Chem.* 70:117–120.

Henry, C. (1998). Dust in the Wind, *Analytical Chemistry News and Features*, July Issue, p. 462A.

Hinz, K-P., Kaufmann, R., and Spengler, B. (1996). Simultaneous Detection of Positive and Negative Ions from Single Airborne Particles by Real-time Laser Mass Spectrometry, *Aerosol Sci. Technol.* 24:233–242.

Knutson, E. O., and Whitby, K. T. (1975). Aerosol Classification by Electric Mobility: Apparatus, Theory, and Applications, *J. Aerosol Sci.* 6:443–451.

Liu, B. Y. H., and Pui, D. Y. H. (1974). Equilibrium Bipolar Charge Distribution of Aerosols, *J. Colloid and Interface Sci.* 49:305–312.

Liu, D-Y., Rutherford, D., Kinsey, M., and Prather, K. A. (1997). Real-Time Monitoring of Pyrotechnically Derived Aerosol Particles in the Troposphere, *Anal. Chem.* 69:1808–1814.

Liu, P., Ziemann, P. J., Kittelson, D. B., and McMurry, P. H. (1995a). Generating Particle Beams of Controlled Dimensions and Divergence: I. Theory of Particle Motion in Aerodynamic Lenses and Nozzle Expansions, *Aerosol Sci. Technol.* 22:293–313.

Liu, P., Ziemann, P. J., Kittelson, D. B., and McMurry, P. H. (1995b). Generating Particle Beams of Controlled Dimensions and Divergence: Ii. Experimental Evaluation of Particle Motion in Aerodynamic Lenses and Nozzle Expansions, *Aerosol Sci. Technol.* 22:314–324.

Morrical, B. D., Fergeson, D. P., and Prather, K. A. (1998). Coupling Two-Step Laser Desorption/Ionization with Aerosol Mass Spectrometry for the Analysis of Individual Organic Particles, *J. Amer. Soc. For Mass Spectr.* 9:1068–1073.

Murphy, D. M., and Thomson, D. S. (1995). Laser Ionization Mass Spectroscopy of Single Aerosol Particles, *Aerosol Sci. Technol.* 22:237–249.

Murphy, D. M., and Thomson, D. S. (1997a). Chemical Composition of Single Aerosol Particles at Idaho Hill: Positive Ion Measurements, *J. Geophys. Res.* 102:6341–6352.

Murphy, D. M., and Thomson, D. S. (1997b). Chemical Composition of Single Aerosol Particles at Idaho Hill: Negative Ion Measurements, *J. Geophys. Res.* 102:6353–6368.

Murphy, D. M., Thomson, D. S., and Mahoney, M. J. (1999). In Situ Measurements of Organics, Meteoritic Material, Mercury, and Other Elements in Aerosols at 5 to 19 Kilometers, *Science* 282:1664–1669.

Noble, C. A., and Prather, K. A. (1996). Real-Time Measurement of Correlated Size and Composition Profiles of Individual Atmospheric Aerosol Particles, *Environ. Sci. Technol.* 30:2667–2680.

Noble, C. A., and Prather, K. A. (1997). Real-Time Monitoring of a Relative Increase in Marine Aerosol Concentration During Winter Rainstorms, *Geophys. Res. Lett.* 24:2753–2756.

Press, W. H., Teukolsky, S. A., Vetterling, W. T., Flannery, B. P. (1998). *Numerical Recipies*: *The Art of Scientific Computing*, Cambridge University Press, New York.

Reilly, P. T. A., Gieray, R. A., Whitten, W. B., Ramsey, J. M. (1998). Real-Time Characterization of the Organic Composition and Size of Individual Diesel Engine Smoke Particles, *Environ. Sci. Technol.* 32:2672–2679.

Salt, K., Noble, C. A., Prather, K. A. (1996). Aerodynamic Particle Sizing Versus Light Scattering Intensity Measurements as Methods for Real-Time Particle Sizing Coupled with Time-of-Flight Mass Spectrometry, *Anal. Chem.* 68:230–234.

Schreiner, J., Voigt, C., Mauersberger, K., McMurry, P., Ziemann, P. (1998). Aerodynamic Lens System for Producing Particle Beams at Stratospheric Pressures, *Aerosol Sci. Tech.* 29:50–56.

Seinfeld, J. H. (1998). Clouds, Contrails and Climate, *Nature* 391:837.

Silva, P. J., and Prather, K. A. (1997). On-Line Characterization of Individual Particles from Automotive Emissions, *Environ. Sci. Technol.* 31:3074–3080.

Sinha, M. P., Giffin, C. E., Norris, D. D., Estes, T. J., Vilker, V. L., and Friedlander, S. K. (1982). Particle Analysis by Mass Spectrometry, *J. Colloid and Interface Science* 87:140–153.

Ziemann, P. J., Liu, P., Rao, N. P., Kittleson, D. B., and McMurry, P. H. (1995). Particle Beam Mass Spectrometry of Submicron Particles Charged to Saturation in an Electron Beam, *J. Aerosol Sci.* 26:745–756.

Received November 19, 1998; accepted June 8, 1999.